Orientation, location, and velocity of Saturn's bow shock: Initial results from the Cassini spacecraft

N. Achilleos,[1] C Bertucci,[1] C. T. Russell,[2] G. B. Hospodarsky,[3] A. M. Rymer,[4] C. S. Arridge,[1] M. E. Burton,[5] M. K. Dougherty,[1] S. Hendricks,[6] E. J. Smith,[5] and B. T. Tsurutani[5]

[1]   The Cassini spacecraft commenced its tour of the planet Saturn on 1 July 2004 (GMT). During the insertion orbit, the Cassini magnetometer (MAG), radio/plasma wave experiment (RPWS), and plasma spectrometer (CAPS) obtained in situ measurements of the magnetic field and plasma conditions associated with Saturn's environment. Analysis of the magnetic field data indicate that Cassini repeatedly crossed a mainly quasi-perpendicular bow shock boundary on both the inbound (post-dawn) and outbound (predawn) legs. Modeling of the bow shock and magnetopause crossing positions shows evidence for a magnetospheric compression during Cassini's immersion in the magnetosphere. The magnetic signatures of the bow shock crossings show the clearly defined "overshoot" and "foot" regions associated with the quasi-perpendicular geometry. The duration of the shock foot, considered in combination with the RPWS and CAPS solar wind electron parameters upstream of the bow shock crossings, indicates that the length scale for the bow shock ramp at Saturn is about an ion inertial length. This is consistent with multispacecraft observations of the spatial scale of the Earth's shock foot region. The data are generally consistent with Saturn bow shock velocities up to $\sim$400 km s^{-1} and shock structures governed by ion dynamics.

1.   Introduction

[2]   The insertion into orbit of the Cassini spacecraft at the planet Saturn on 1 July 2004 (UTC) initiated the extended campaign of observations that an orbiter can provide, enabling a statistical picture rather than "snapshots" of the various boundaries and regions of Saturn's magnetosphere. The Cassini magnetometer (MAG) [*Dougherty et al.*, 2004] provides continuous monitoring of the magnetic field associated with Saturn's internal source and plasma environment. Magnetic data acquired during the orbiter's tour of the planet (2004–2008) will be essential for studying, among other aspects, the interaction between the solar wind and Saturn's magnetosphere. In this study, we analyze magnetic data and electron plasma data in order to charac-terize the orientation, length scale and motion of Saturn's bow shock.

[3]   Saturn's magnetosphere presents an obstacle to the solar wind flow far larger than the planetary body alone. The subsolar magnetopause lies distances $\sim$20 R$_S$ (1 R$_S$ = Saturn radius = 60330 km) from the planet. The solar wind plasma impinging on the magnetospheric obstacle is decel-erated by the bow shock, across which the plasma's physical parameters change abruptly. The magnetic signature of the bow shock observed by spacecraft is largely controlled by the angle θ_{BN} between the upstream (solar wind) magnetic field and the local normal to the bow shock surface. The most abrupt and distinct changes in field strength are associated with quasi-perpendicular regions where $\theta_{BN} \gg 45°$, while quasi-parallel areas of the shock surface ($\theta_{BN} \ll 45°$) generally exhibit a much broader, more disturbed magnetic transition (see the reviews by *Burgess* [1995] and *Walker and Russell* [1995]).

[4]   The observed magnetic structure of a bow shock transition between the solar wind and magnetosheath is also influenced by the upstream plasma β (ratio of thermal to magnetic pressure), which affects the level of turbulence seen in the magnetosheath [*Farris et al.*, 1992]; and by the magnetosonic Mach number M$_{MS}$ of the solar wind flow [*Russell et al.*, 1982]. A strong shock, like that of Saturn, converts much of the solar wind momentum flux into the thermal energy of the downstream plasma.

[1]Blackett Laboratory, Imperial College, London, UK.
[2]UCLA Institute of Geophysics and Planetary Physics, Los Angeles, California, USA.
[3]Department of Physics and Astronomy, University of Iowa, Iowa City, Iowa, USA.
[4]Mullard Space Science Laboratory, University College, London, UK.
[5]Jet Propulsion Laboratory, California Institute of Technology, Pasadena, California, USA.
[6]Institute of Geophysics and Meteorology, University of Cologne, Cologne, Germany.

[5] A physically important flow parameter is the critical Mach number M_C. When the upstream Mach number M_{MS} exceeds M_C, the downstream flow speed becomes greater than downstream sound speed [*Kennel et al.*, 1985] and the shock is called supercritical. The magnetic structures and energy dissipation of supercritical shocks are inherently different from those of the subcritical regime. The majority of encounters reported in this study are quasi-perpendicular, supercritical bow shocks. The data are in agreement with the picture of a magnetic profile that is determined by ion kinetics. The general features include a "foot" region of upstream turbulence and gradual increase in field strength, which immediately precedes the shock ramp where the most abrupt change in magnetic field strength occurs. There is also, usually, a strong "overshoot" in field strength in the region immediately downstream of the ramp.

[6] The spatial scale of the foot region for supercritical, quasi-perpendicular shocks is expected to be equal to the mean radius of curvature, or "turn-around distance," associated with the paths of specularly reflected ions emerging from the bow shock and returning to the solar wind [*Gosling and Thomsen*, 1985]. Multispacecraft observations at the Earth have revealed that the length scale of the ramp for these types of shocks is typically a few tenths of the ion inertial length c/ω_{pi} (ratio of light speed to ion plasma frequency) [e.g., *Newbury and Russell*, 1996; *Russell and Greenstadt*, 1979; *Scudder et al.*, 1986]. Interestingly, *Newbury and Russell* [1996] reported an unusually thin shock ramp in their sample of Earth observations, whose thickness was approximately two electron inertial lengths. This thin shock was suspected to result from the transition into the perpendicular regime ($\theta_{BN} = 90°$), where electron kinetics become important in determining shock structure [e.g., *Savoini and Lembege*, 1994].

[7] The global shape of planetary bow shocks is frequently approximated by models with a hyperboloid geometry (conic section with eccentricity larger than unity), whose focus is at or near the planet center. Such models also usually have rotational symmetry about the direction of the upstream solar wind velocity relative to the planet center. At Saturn, this direction deviates from the Saturn-Sun line by less than 3 degrees. The most comprehensive empirical modeling of Saturn's bow shock surface to date was done by *Slavin et al.* [1985], who used the locations of bow shock encounters from the Voyager and Pioneer flybys to fit a hyperbolic surface model, with a high degree of downstream flaring. This model was then rescaled in size, in order to derive instantaneous standoff distances for individual bow shock crossings (standoff distance is the distance between Saturn centre and the subsolar point, or "nose," of the bow shock). This information was used in turn to derive an empirical relation between the shock standoff distance R_{SN} and the solar wind dynamic pressure P_{SW} (obtained from spacecraft plasma measurements).

[8] A comprehensive study of Saturn's global bow shock geometry and its dependence on solar wind conditions, using Cassini data, would require: (1) a set of spacecraft orbits which sample the bow shock surface at as many different local times and latitudes as possible; and (2) plasma measurements of the solar wind dynamic pressure, where possible. We intend to pursue such a study as more coincident magnetic and plasma data sets become available. However, it

is beyond the scope of the current work, which concentrates on the magnetic bow shock encounters observed during the insertion orbit of Cassini (in particular, days 179, 180 and 189 through 196 of year 2004).

[9] Bulk velocity measurements of the solar wind ions are not easily obtainable for this interval, as the spacecraft orientation during Saturn orbit insertion (SOI) was constrained by critical engineering requirements, and was not optimal for CAPS observations of solar wind velocity. In addition, there was an outage of spacecraft science telemetry during days 186 through 192 of the SOI outbound leg. However, magnetic bow shock detections were still possible during most of this period, using the lower resolution (4 s) measurements from the vector helium magnetometer (VHM) which are routinely downlinked in the engineering telemetry for the MAG instrument.

[10] For the current study (section 3), we consider electron plasma measurements of the solar wind densities obtained from RPWS plasma wave frequencies and temperatures derived from CAPS electron spectra (more details of these experiments are given by *Gurnett et al.* [2004] and *Young et al.* [2004]). These plasma moments for the SOI inbound leg are used in conjunction with established geometric models for Saturn's bow shock surface, in order to estimate the temporal variation in the global size of the bow shock itself, as well as to model the corresponding change in the solar wind velocity. We then compare the theoretical and observed orientations of the local bow shock surface at the locations of the shock crossings. This is done by comparing the surface normal vectors at these crossings predicted by the geometrical models with those derived from a coplanarity analysis of the magnetic upstream and downstream data (section 4).

[11] Finally, in section 5, we examine the smaller-scale structure of the bow shock. We make the assumptions of: (1) a fixed value for the solar wind velocity, consistent with the mean values detected by the Pioneer spacecraft and the model values obtained in the current study; and (2) a spatial scale for Saturn's shock foot region equal to the theoretical value, of the order of the ion convective gyroradius (in the shock rest frame) associated with solar wind ions reflected from the bow shock back into the upstream region. By making these specific and plausible assumptions, we are able to use the observed duration in time of the shock foot in order to estimate the velocity of the shock surface at the locations of the relevant crossings. We find that the time dependence of the observed magnetic profiles is almost entirely determined by the motion of the bow shock itself, and not by the motion of the spacecraft. The shock velocities thus derived are of order between 10 and 100 km s^{-1}, indicating a highly dynamic bow shock surface, most likely due to variability in the physical conditions of the upstream solar wind.

2. Observations

[12] We begin by considering the magnetic field observed by the vector helium magnetometer (VHM) during the inbound and outbound legs of the Cassini insertion orbit. The Cartesian components of the field in the KSM (Kronocentric Solar Magnetospheric) coordinate system were presented by *Dougherty et al.* [2005]. This is the
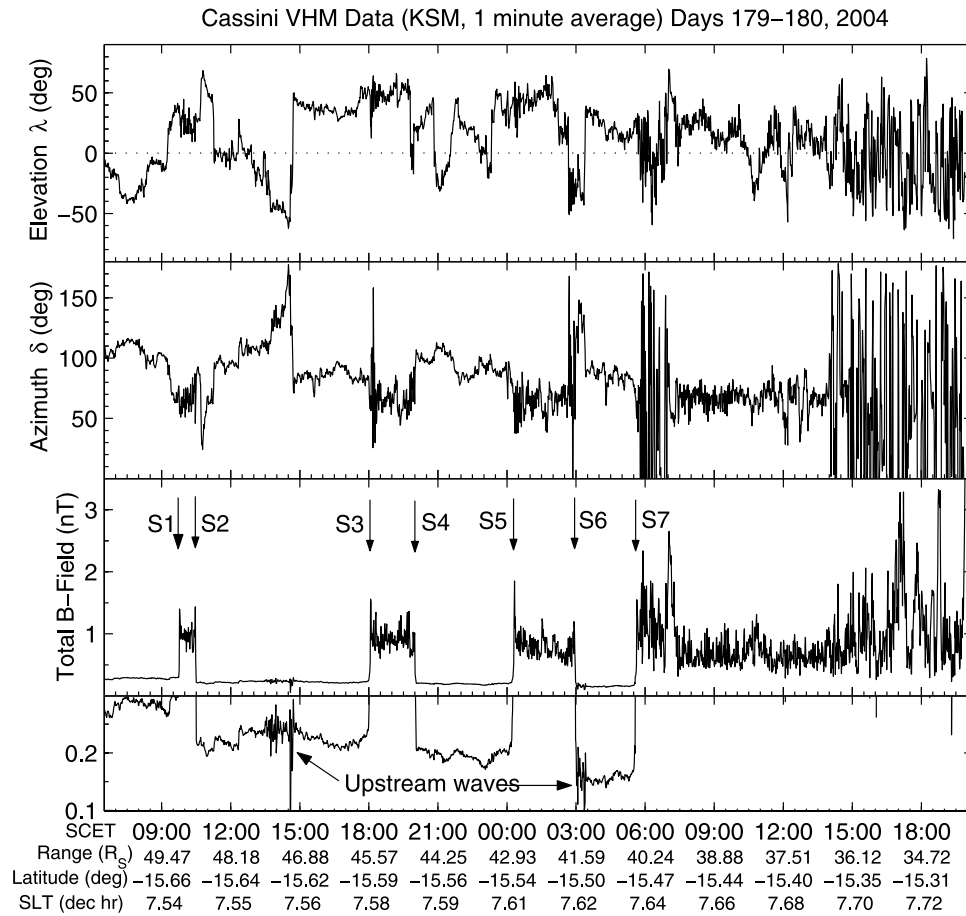
Figure 1. Magnetic orientation and strength measured by the VHM during the inbound pass of the SOI orbit. The angles λ and δ are the field elevation and azimuth with respect to KSM coordinates (see text). Bow shock crossings are labeled, and examples of upstream wave intervals are shown in the bottom panel. The horizontal axis shows spacecraft event time (SCET), which is Universal Time Coordinate (UTC) corresponding to the actual time at which the field measurement was acquired. Also shown are the spacecraft distance from Saturn center (range) in Saturn radii (R_S); the latitude with respect to Saturn's equatorial plane; and the spacecraft's local time with respect to Saturn (SLT) in decimal hours, where 24 hours corresponds to one planetary rotation period.

orthogonal, Saturn-centered coordinate system in which the positive X axis points toward the Sun, and the Z axis is chosen so that the XZ plane contains Saturn's magnetic dipole axis (herein assumed to be parallel to the planet's rotation axis, consistent with the current value of $<1°$ for the angle between Saturn's dipole and rotational axes [*Smith et al.*, 1980a; *Connerney et al.*, 1983; *Dougherty et al.*, 2005]). During the SOI interval shown, Saturn's dipole axis was tilted at an angle of approximately 25° antisunward with respect to the Z (KSM) axis. During the same time period, the XY plane of the KSM system was oriented at approximately 11° to Saturn's orbital plane (both planes intersecting along the X axis).

[13] In Figures 1 through 3, we show the total field strength and orientation with respect to the KSM coordinates, as measured by the Vector Helium Magnetometer (VHM), for the SOI inbound and outbound legs. We specify field orientation with two angles. These are: (1) the field elevation λ, which is the angle between the field vector and its projection onto the XY plane (positive λ indicates field with positive Z component); and (2) the field azimuth δ,

which is the angle between the antisunward direction and the projection of the field onto the XY plane (increasing toward the direction of Saturn's orbital velocity). The orientation of the nominal Parker spiral at the location of Saturn's orbit would have values of δ close to 90° or 270°.

[14] Figure 1 shows the seven bow shock crossings identified by *Dougherty et al.* [2005] on the SOI inbound pass. The solar wind excursions during this time interval have values of δ mostly between $\sim$70° and 120°. Notable exceptions are the indicated brief ($<$2 hours) intervals when the spacecraft observed magnetic signatures of plasma waves upstream from the bow shock itself. The field during the wave observations has much larger values of δ: almost 180° for the region between crossings S2 and S3. These waves are therefore seen when the spacecraft is situated on field lines which are adequately close to the Saturn-Sun direction to be magnetically connected to the bow shock surface. The most likely explanation for this is that the waves are generated by solar wind particles being reflected back upstream from the quasi-perpendicular bow shock regions; or by energetic magnetospheric particles escaping
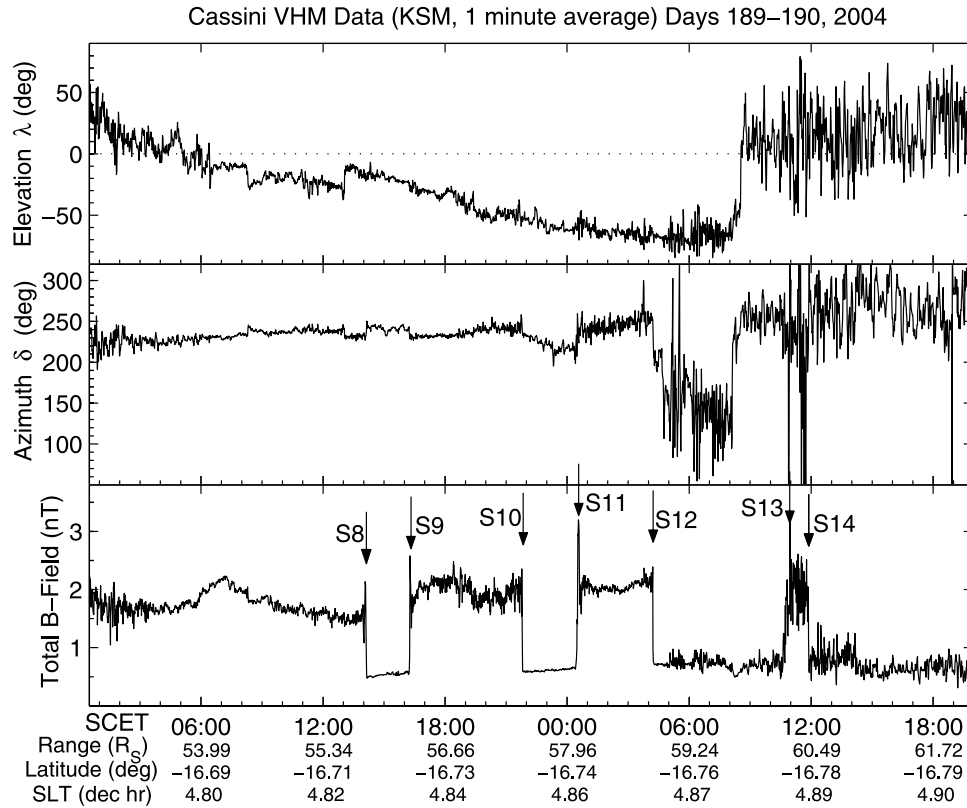
Figure 2. Magnetic orientation and strength measured by the VHM during the first part of the outbound pass of the SOI orbit. The angles λ and δ are the field elevation and azimuth with respect to KSM coordinates (see text). Bow shock crossings are labeled, and the horizontal axis is labeled using the same scheme as for Figure 1.

upstream into the solar wind. The upstream wave signatures and their correlation with the field orientation and shock geometry are further analyzed by C. Bertucci et al. (manuscript in preparation, 2005). Signatures of upstream Langmuir waves were also observed by RPWS during these time intervals on day 179, implying the presence of electrons streaming from the bow shock.

[15] The magnetic profiles of the bow shock crossings in Figure 1 are all consistent with the "clean," relatively abrupt transitions associated with traversal of a quasi-perpendicular shock. This is verified by the coplanarity analysis described in section 4, which yields values of $40°$–$70°$ for the angle θ_{BN} between the solar wind magnetic field and the local normal to the shock surface. The field azimuth δ has values during the magnetosheath intervals which are typically $\sim30°$ smaller than those of the solar wind excursions. This is the remote "draping" (rotation toward antisunward direction) of the field, which is embedded in solar wind plasma that has been decelerated after its passage through the bow shock into the magnetosheath. The magnetosheath field is also very disturbed immediately following crossing S7 and also when the spacecraft is closer than ~37 R_S to the planet, making its first brief excursions into the magnetosphere [*Dougherty et al.*, 2005].

[16] Figures 2 and 3 show the behavior of the magnetic field sampled by the spacecraft during the outbound pass of the SOI orbit. Most of the bow shock crossings seen here in the predawn sector of the planet are quasi-perpendicular

($\theta_{BN} > 50°$, section 4). One exception is S18, for which the shock normal derived from coplanarity indicates $\theta_{BN} < 20°$, an apparently quasi-parallel geometry. This angle cannot be considered definitive, however, given that the coplanarity technique is inaccurate for small θ_{BN} (close to parallel), and that S18 is probably a nonstationary shock transition (section 4). S18 is preceded by crossings S16p and S17p, whose nomenclature denotes that they were clearly seen in the electron plasma data from the Cassini plasma spectrometer (CAPS) and from the Cassini radio and plasma wave experiment (RPWS). These two crossings are not as clearly discernible in the MAG data as the abrupt changes in field strength associated with the quasi-perpendicular shocks. They are highly turbulent and extended transitions, probably corresponding to a quasi-parallel geometry. The appearance of quasi-parallel crossings on the outbound pass is not surprising, given that the bow shock surface models predict smaller values of θ_{BN} for regions further downstream of the nose (section 3).

[17] Crossings S13, S14 and S19 were not suitable for coplanarity analysis; their highly variable magnetic signatures precluded straightforward identification of subintervals representative of stationary upstream (solar wind) and downstream (magnetosheath) magnetic fields. The magnetic field in both the solar wind and the magnetosheath becomes noticeably more disturbed following S12, which may be the signature of a significant "rearrangement" of the magnetosheath flow in response to a change in the configuration
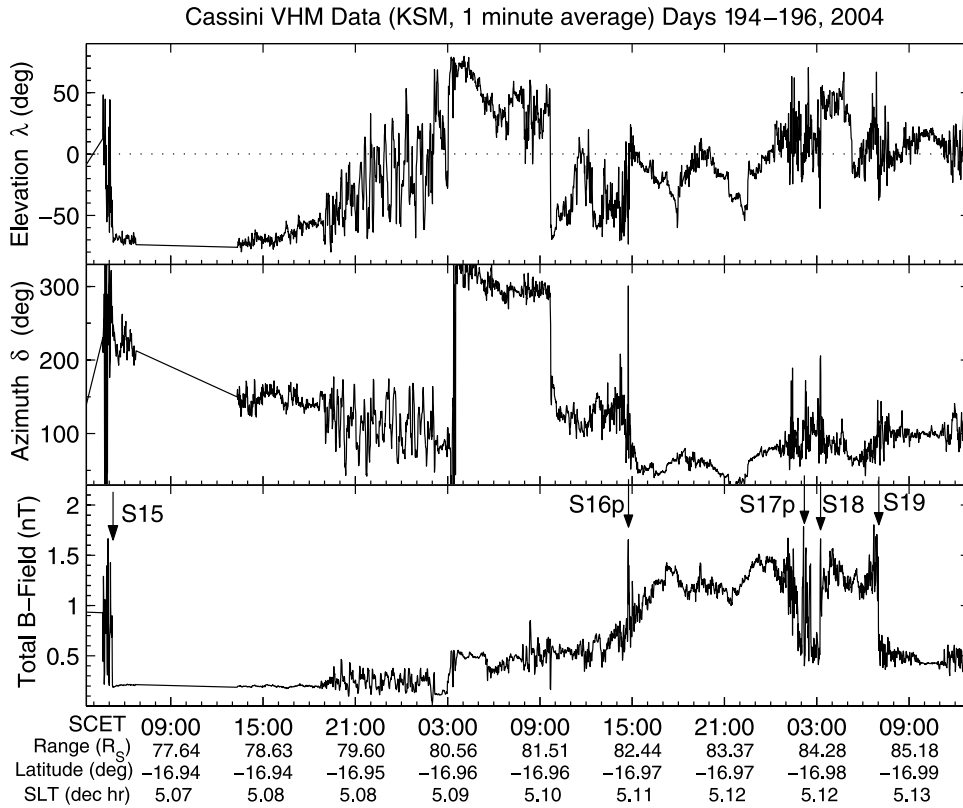
Figure 3. Magnetic orientation and strength measured by the VHM during the second part of the outbound pass of the SOI orbit. The angles λ and δ are the field elevation and azimuth with respect to KSM coordinates (see text). Bow shock crossings are labeled, and the horizontal axis is labeled using the same scheme as for Figure 1. There is a gap in the data between 07:00 and 13:00 on Day 194.

of the magnetosphere (see also section 3). There is also a persistent change of $\sim180°$ in the angle δ at around 0900 UTC on day 195, corresponding to the spacecraft crossing the heliospheric current sheet.

3. Boundary Locations and Magnetospheric Dynamics

[18] It is a well-established fact that multiple bow shock and magnetopause crossings, usually seen by spacecraft traversing planetary magnetospheres, are generally the result of the rapid motion of these boundaries relative to the spacecraft (although multiple magnetopause encounters may often result from wave-like disturbances propagating along this boundary, such as those seen at Saturn by *Lepping et al.* [1981]). Bow shock encounters are generally seen over a larger range of distances than those of the magnetopause, reflecting the greater sensitivity of the bow shock's standoff distance to changes in the properties of the solar wind. In addition to the dynamic pressure of the solar wind, the shock location depends on the Mach number of the solar wind plasma and the direction of the interplanetary magnetic field. If all this variation is ascribed to the solar wind dynamic pressure as in the study of the Voyager and Pioneer encounters by *Slavin et al.* [1985], then the dependence will be weakened. In particular, *Slavin et al.* [1985] found that the standoff distances of the planet's bow shock

varied in proportion to $P_{SW}^{-1/5.1}$, as compared to $P_{SW}^{-1/6.1}$ for the magnetopause.

[19] To further investigate the motion of Saturn's bow shock and magnetopause during the Cassini insertion orbit, we may adapt the technique employed by *Joy et al.* [2002]. For the planet Jupiter, these authors examined many orbits of spacecraft which had explored the Jovian environment. The distribution of relative time intervals spent by the spacecraft in the solar wind, magnetosheath, and magnetosphere regions enabled the identification of the most probable locations of Jupiter's bow shock and magnetopause boundaries.

[20] For the Cassini data acquired at Saturn orbit insertion, we have calculated the durations of the time intervals (excursions) observed by the spacecraft in these same regions. They are shown as a function of the median (central) time for each excursion in Figure 4. Calculation of excursion times was not always possible in a continuous manner, owing to intermittent gaps in spacecraft telemetry during the outbound pass on days 191 through 194.

[21] Despite the data not being available for all times, it is possible to identify, to first order, the times at which the spacecraft observed excursions of equal duration in the solar wind and in the magnetosheath. A simple linear interpolation of the data points in Figure 4 reveals that these times of solar wind/magnetosheath transition occurred on day 180 at UTC 02:00 (±3 hours), day 190 at 02:00 (±4 hours) and (using linear extrapolation) day 195 at 06:00 (±1 day). The
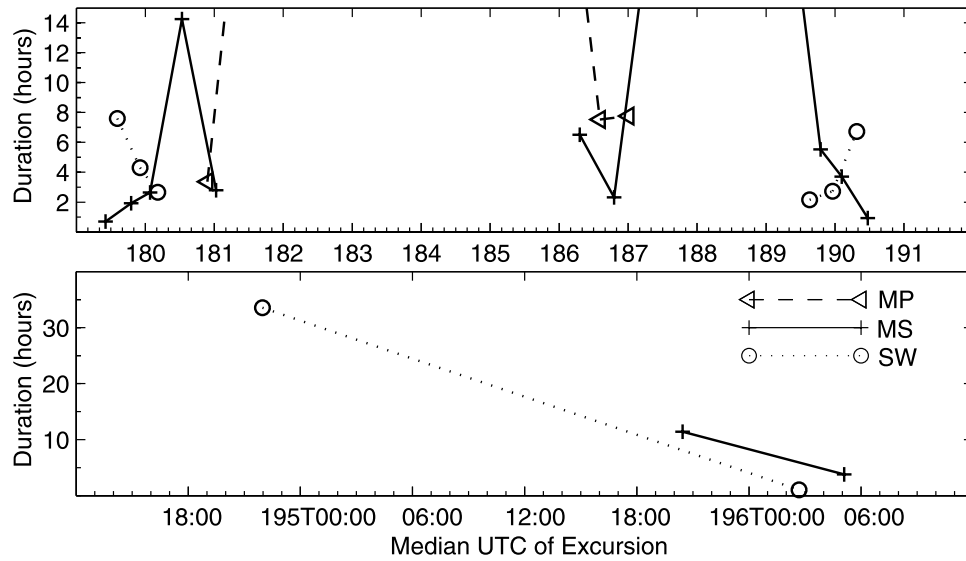
Figure 4. Duration of excursions by Cassini into the solar wind (SW), magnetosheath (MS), and magnetosphere (MP). The length of each excursion is plotted as a function of its median (central) time. The incomplete coverage is due to intermittent gaps in spacecraft telemetry during the outbound pass, on days 191 through 194.

quoted uncertainties are an indication of the time resolution with which these transitions can be located; they correspond to the equal length of magnetosheath and solar wind excursions at the points of intersection of the linear fits shown in Figure 4 for these regions. These results therefore indicate at least two such transition regions on the outbound pass, compared to the single transition on the inbound leg.

[22] The segments of the spacecraft trajectory traversed during the identified transition periods between the solar wind and the magnetosheath (SW/MS) are represented in Figure 5, as thick grey arcs slightly displaced (for clarity) from the main trajectory. The analogous transition regions between the magnetosheath and magnetosphere (MS/MP) are shown as thick black arcs in Figure 5. An examination of the magnetosheath and magnetosphere excursions in Figure 4 shows that there is one discernible transition (location of equally long excursion times) between these two regions on approach to the planet, and a second transition on the outbound leg. The locations of the magnetic bow shock and magnetopause crossings are also shown in Figure 5, in the cylindrical KSM system (where the Y_{KSM} and Z_{KSM} coordinates have been collapsed into a single distance, measured perpendicular to the X_{KSM} axis).

[23] Figure 5 also features a selection of model surfaces for Saturn's bow shock and magnetopause. These can be used to estimate the standoff distances for bow shock and magnetopause surfaces which intersect the locations of the identified SW/MS and MS/MP transition regions. The magnetopause models shown in the plot are as follows.

[24] 1. "Model S_{MP}" is based on the empirical model computed by *Slavin et al.* [1985] through fitting a (nearly paraboloid) surface to the Voyager and Pioneer crossings of Saturn's magnetopause. The equation for this surface model, which is assumed here to be symmetric about the X axis (Saturn-Sun line), is $r = L/(1 + \varepsilon \cos \varphi)$ (*Slavin et al.* [1985] used an axis of symmetry parallel to the solar wind velocity relative to Saturn, which is <3 degrees from the X axis for

typical solar wind speeds). r is distance from the focus of the surface (the point $(X, Y, Z) = (x_O, 0, 0)$); ε is the eccentricity (determines shape, $\varepsilon \sim 1$ for "streamlined," increasing ε representing a more flared or "blunt" obstacle); L is the size parameter, which may be varied (at fixed x_O and ε) in order to perform a self-similar "rescaling" of the model [*Slavin et al.*, 1985]; and $\cos \varphi = (X_s - x_O)/r$ where X_s denotes the KSM X coordinate of a point on the model surface. For Model S_{MP}, $\varepsilon = 1.09$ and $x_O = 5$ R_S (taken from *Slavin et al.*'s [1985] magnetopause fit with correction for variability in solar wind dynamic pressure). The size parameter L has been chosen to produce a model which passes through the location of the MS/MP1 transition region on the inbound pass. When the model is "rescaled" as described, there is a correspondence between L, standoff distance and solar wind dynamic pressure (P_{SW}). For example, Model S_{MP} with $L = 30.8$ R_S was used by *Slavin et al.* [1985] for fitting pressure-corrected magnetopause crossings, and their work shows that a model of this size has a standoff distance of $R_{MP} = x_O + L/(1 + \varepsilon) = 19.7$ R_S and corresponds to $P_{SW} = 0.02$ nPa. This relationship between standoff distance and P_{SW} is explored further later in this section.

[25] 2 "Model MEBS" is the theoretical model computed by *Maurice et al.* [1996], who applied a balance condition at the magnetopause between solar wind dynamic pressure P_{SW} and the magnetic pressure inside the magnetopause. This allowed the simultaneous determination of the magnetopause geometry and the magnetospheric field. The global size of the model is set by the choice of standoff distance R_{MP}, and for the plot we have chosen R_{MP} to produce a "rescaled" model which passes through the inbound transition region MS/MP1.

[26] The bow shock models shown in the same plot are as follows.

[27] 1. "Model S_{BS}" is based on the empirical model computed by *Slavin et al.* [1985] by fitting a hyperboloid surface to the Voyager and Pioneer crossings of Saturn's
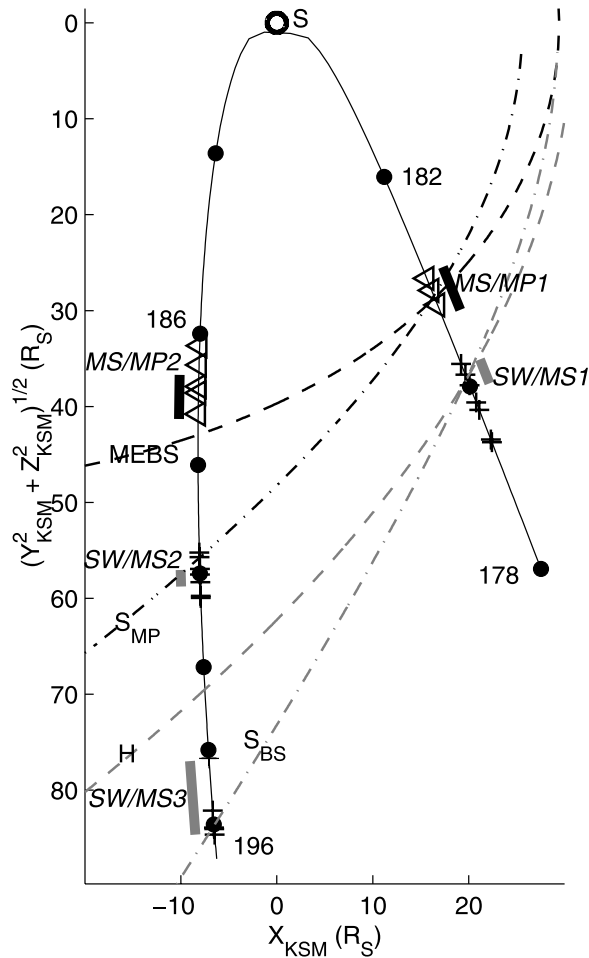
Figure 5. Bow shock (crosses) and magnetopause (triangles) crossings during the SOI orbit (solid curve), projected into cylindrical KSM coordinates (see text). The spacecraft trajectory is labeled with time ticks (solid circles) which are separated by 2 days; the day of year labels shown for some ticks correspond to that day's beginning (i.e., zero hours UTC). The thick lines near the orbit show the transition regions between the magnetosphere and magnetosheath (black); and between the magnetosheath and solar wind (gray). The surface models shown are: Models S_{BS} and S_{MP} by *Slavin et al.* [1985] for the bow shock (gray dash-dotted line) and magnetopause (black dash-dotted line); Model MEBS for the magnetopause by *Maurice et al.* [1996]; and Model H for the bow shock by *Hendricks et al.* [2005]. All models have been scaled in a self-similar manner, in order to intersect the mean location of the appropriate inbound transition regions.

bow shock. The general equation, as for Model S_{MP}, is a conic section rotated about the X axis. Model S_{BS} has $\varepsilon =$ 1.71 and $x_O = 6$ R_S. The size parameter L has been chosen, for plotting purposes, to give a version of the model which passes through the inbound transition region SW/MS1.

[28] 2. "Model H" is computed by *Hendricks et al.* [2005], from "building" a theoretical hyperboloid bow shock surface about a "core" magnetopause, the latter being derived from the model by *Maurice et al* [1996]. This

construction employed the relation of *Petrinec and Russell* [1997] between the bow shock standoff distance and the radius of curvature of the subsolar magnetopause. The average downstream shape of Model H was constrained by requiring the tangent of the asymptotic Mach cone angle to approach $1/M_{MS}$, where M_{MS} is the upstream magnetosonic Mach number, derived from plasma observations in the solar wind by the spacecraft considered in the study (Voyagers 1 and 2, Pioneer 11, Ulysses) . Model H has $\varepsilon =$ 1.02 and $x_O = 0$. The size parameter L for Model H in the plot has been chosen to give a "rescaled" model passing through the SW/MS1 transition.

[29] Models S_{MP} and S_{BS} are considerably more flared than Models MEBS and H (respectively), especially in the region downstream of the planet ($X < 0$). *Slavin et al.* [1985] pointed out that their model fits (S_{MP} and S_{BS}) for Saturn were not well constrained in the region $X < \sim-10$ R_S, owing to the paucity of data there. Model S_{BS} has a high eccentricity ($\varepsilon = 1.71$, hyperbolic) compared to Model H ($\varepsilon =$ 1.02, nearly parabolic), while eccentricities of $1.1-1.4$ are typically observed for the Earth's bow shock [e.g., *Maksimovic et al.*, 2003]. The MEBS model for Saturn's magnetopause is not based on a conic fit, but is clearly more "streamlined" than Model S_{MP}. Future orbits of the Cassini spacecraft, which sample the magnetotail and downstream regions of the bow shock and magnetopause, should provide important observational evidence of the actual degree of downstream flaring for these boundaries, which is related to the physical processes responsible for their formation. A more detailed analysis by C. S. Arridge et al. (Modeling the size and shape of Saturn's magnetopause with variable dynamic pressure, submitted to *Journal of Geophysical Research*, 2006) (hereinafter referred to as Arridge et al., submitted manuscript, 2006) derives a power law, using Model MEBS, for magnetopause standoff distance versus solar wind dynamic pressure. A new pressure-corrected surface model is then derived by these workers, which highlights the nature of the downstream flaring of the magnetopause boundary in more detail.

[30] Table 1 shows the results of rescaling the models, as described above, to assign standoff distances for the bow shock (R_{SN}) and magnetopause (R_{MP}), on the basis of the requirement that the rescaled models pass through the locations of the SW/MS and the MS/MP transitions listed, and indicated in Figure 4 and 5.

[31] Table 1 also shows the predicted solar wind dynamic pressures P_{SW} associated with the calculated standoff distances. For the magnetopause models MEBS and S_{MP}, values of P_{SW} were calculated by using the empirical relation $R_{MP} \propto P_{SW}^{(-1/6.1)}$ determined by *Slavin et al.* [1985] from Voyager/Pioneer plasma and magnetic measurements. It is important to note in this context that concurrent work by Arridge et al. (submitted manuscript, 2006) indicates that this power law is consistent with the equivalent relation derived from applying Model MEBS to a more extensive data set (five orbits) of Cassini magnetopause crossings. However, Arridge et al.'s work also shows that the power law index in this relation lies between $-1/4$ and $-1/5$ when a shape model for the magnetopause with pressure-dependent geometry is independently derived, probably indicative of a "stretched" configuration of magnetic field lines in the outer magnetosphere.

Table 1. Transition Regions Between Solar Wind and Magnetosheath and Between Magnetosheath and Magnetosphere[a]

Transition, UTC	Range to Saturn, R_S	Saturn Local Time, hh:mm	Latitude, deg	R_{MP} (Model S_{MP}), R_S	R_{MP} (Model MEBS), R_S	P_{SW} (Model S_{MP}), nPa	P_{SW} (Model MEBS), nPa	P_{SW} (Pressure Balance), nPa
MS/MP1 D180T22:00	32.83	07:45	-15.24	25.6	29.4	0.0033 ± 20%	0.0014 ± 20%	0.025 ± 40%
MS/MP2 D186T22:00	39.92	04:34	-16.39	17.9	26.8	0.03 ± 30%	0.0025 ±20 %	0.072 ± 30%

Transition, UTC	Range to Saturn, R_S	Saturn Local Time, hh:mm	Latitude, deg	R_{SN} (Model S_{BS}), R_S	R_{SN} (Model H), R_S	P_{SW} (Model S_{BS}), nPa	P_{SW} (Model H), nPa
SW/MS1 D180T02:00	42.04	07:37	-15.52	29.3	30.8	0.018 ± 65%/30%	0.007 ± 45%
SW/MS2 D190T02:00	58.39	04:52	-16.75	19.1	24.9	0.158 ± 160%/60%	0.025 ± 40%
SW/MS3 D195T06:00	81.04	05:06	-16.96	28.1	36.7	0.022 ± 90%/50%	0.003 ± 50%

[a]Solar wind, SW; magnetosheath, MS; magnetosphere, MP. The UTC time of observation for each transition is shown, along with the spacecraft's range (distance from Saturn center), local time at Saturn, and planetocentric latitude. The bow shock/magnetopause standoff distances (R_{SN}, R_{MP}) and the solar wind dynamic pressures (P_{SW}) implied by the transitions are also shown, labeled with the models used for their calculation.

[32] Returning to the principal magnetopause models MEBS and S_{MP} used in this study, the relative uncertainty in P_{SW} indicated for these models in Table 1 is equivalent to the variation in P_{SW} corresponding to a change in R_{MP} equal to the r.m.s. residual distance (0.87 R_S) for the two-dimensional (2-D) magnetopause surface fit derived by *Slavin et al.* [1985]. We see that model S_{MP} requires a relatively strong magnetospheric compression to explain the relative positions of the inbound and outbound MS/MP transitions. Specifically, the S_{MP} model predicts an increase in P_{SW} by a factor of at least 5 between MS/MP1 and MS/MP2, corresponding to a decrease of ~8 R_S in magnetopause standoff distance R_{MP}. Model MEBS, on the other hand, because it is significantly less flared than S_{MP}, can explain the observed transitions through a much smaller compression involving a factor of ~1.8 increase in P_{SW} and a decrease of ~2.5 R_S in R_{MP}. It is immediately apparent that the nature of magnetospheric dynamics obtained through the use of bow shock and magnetopause surface models is very sensitive to their geometries. It is therefore of great importance to constrain such models further (especially in the region $X < \sim{-}10$ R_S) using future Cassini observations.

[33] To emphasize this point, we have included in Table 1 (Pressure Balance column) the range of values of P_{SW} from the study by Arridge et al. (submitted manuscript, 2006), which were derived empirically at each magnetopause crossing, assuming that the combined solar wind dynamic and static (thermal) pressures were balanced by the magnetospheric magnetic pressure just inside the magnetopause (a technique previously used for the case of Saturn by *Slavin et al.* [1985]). It is apparent that these empirical estimates of P_{SW} may exceed the model-dependent values by an order of magnitude. This is possible (but not conclusive) evidence for a magnetosphere which is significantly more compressible, with a more sensitive response of size to pressure than that indicated by the $R_{MP} \propto P_{SW}^{(-1/6.1)}$ relation. This would be consistent with the $R_{MP} \propto P_{SW}^{(-1/4.4)}$ relation of Arridge et al.'s magnetopause model (2005). Moreover, these empirical estimates of P_{SW} for the MS/MP transitions are more continuous, as a function of time, with the solar wind pressure values estimated by the bow shock models for

both the inbound and outbound SW/MS transitions. The empirical P_{SW} value also increases from the inbound to the outbound MS/MP transition, but by a factor of ~3, which lies between the analogous compression factors associated with the S_{MP} and MEBS models.

[34] A similar scenario applies to the bow shock modeling results of Table 1. To obtain P_{SW} values here, we used the empirical relation between P_{SW} and R_{SN} derived by *Slavin et al.* [1985] (model S_{BS}) and by *Hendricks et al.* [2005] (and S. Hendricks, private communication, 2005). Specifically, these are $R_{SN} = 13.33\, P_{SW}^{-1/5.1}$ (model S_{BS}) and $R_{SN} = 13.17\, P_{SW}^{-1/5.79}$ (model H), where R_{SN} is in units of R_S and P_{SW} is in units of nano-Pascal (nPa). The relative uncertainties in P_{SW} for the bow shock models were calculated as follows. For model S_{BS}, this uncertainty equals the variation in P_{SW} corresponding to the r.m.s. residual distance (3.6 R_S) for the 2-D bow shock surface fit derived by *Slavin et al.* [1985]. For model H, the uncertainty in P_{SW} was calculated by propagating the 2.5σ standard errors in the numerical coefficients of the least squares fit for the R_{SN} versus P_{SW} relation.

[35] Interestingly, both models S_{BS} and H are in marginal agreement regarding the P_{SW} value for the inbound SW/MS transition. Comparing this to the first outbound transition SW/MS2, model S_{BS} requires a factor of at least 2 increase in P_{SW}, while model H indicates an increase of >30% in P_{SW}. This is due to the reduced flaring in model H, as well as the somewhat smaller sensitivity of its R_{SN} values to variability in P_{SW}. However, to explain the different position of SW/MS3, the second outbound transition, in relation to SW/MS2, both models predict a significant expansion of the bow shock, with an increase of ~10 R_S in R_{SN}. SW/MS3 corresponds to approximately the same bow shock configuration as SW/MS1, according to model S_{BS}. Model H indicates a marginal expansion between these two transitions, however this is not conclusive, considering the relative uncertainties in P_{SW}. Note that our model predictions for bow shock and magnetopause variability are consistent with the analysis of the interplanetary magnetic field (IMF) by *Jackman et al.* [2005], which predicts a magnetospheric compression at Saturn in the interval be-

Table 2. Properties of Solar Wind Upstream of the First Six Bow Shock Crossings Observed by Cassini[a]

Bow Shock Crossing, UTC (Year 2004)	Range (R_S)	Saturn Local Time, hh:mm	Latitude, deg	V_{SW}^* (Model S_{BS}), km s^{-1}	V_{SW}^* (Model H), km s^{-1}	RPWS N_E, cm^{-3}	CAPS ELS T_E, eV	M_{MS} (for V_{SW} = 400 km s^{-1})	Plasma β
S1 D179T09:46:46	49.14	07:33	-15.66	376 (±30%/15%)	327 (± 20%)	0.038	1.28	10.07	0.25
S2 D179T10:28:34	48.84	07:33	-15.66	381	332	0.038	1.00	14.04	0.44
S3 D1 79T18:04:23	45.54	07:35	-15.59	445	397	0.038	1.70	11.39	0.51
S4 D179T20:00:13	44.69	07:35	-15.57	342	307	0.070	1.70	15.14	1.32
S5 D180T00:18:34	42.79	07:37	-15.53	374	331	0.071	1.50	15.11	1.03
S6 D180T02:57:44	41.61	07:37	-15.51	413	369	0.066	2.00	16.19	2.86
S7 D180T05:37:50	40.41	07:38	-15.47	405	361	0.078	2.00	15.52	2.21
S18 D196T03:12:04	84.31	05:07	-16.98	1321	706	0.006	. . .	. . .	. . .
S19 D196T06:59:12	84.88	05:08	-16.98	819	447	0.015	. . .	. . .	. . .

[a]Model solar wind velocities V_{SW}^* derived from the bow shock models S_{BS} and H are shown. Electron densities (N_E) and temperatures (T_E) derived from RPWS and CAPS data are shown. These were used to compute the magnetosonic Mach number M_{MS} and plasma ratio of thermal to magnetic pressure (β), assuming a solar wind velocity of 400 km s^{-1} appropriate for Saturn, and a pure hydrogen plasma with temperatures as described in the text.

tween days 185 and 189 of 2004 (during the traversal of the magnetosphere by Cassini), followed by a subsequent expansion. This general pattern of dynamics is indicated by both sets of models that we have considered, although with differing degrees of magnetospheric compression and expansion, as described above.

[36] In order to investigate in more detail the physical conditions in the solar wind plasma during SOI, we can make use of electron plasma moments which have been computed to date from CAPS/ELS (electron spectrometer) data and RPWS data. These were acquired from intervals in the solar wind, upstream (between 3 min and 1.25 hours) of the seven inbound bow shock crossings and two of the outbound crossings. These electron densities and temperatures are shown in Table 2, along with the bow shock crossings to which they correspond.

[37] The entries in Table 2 marked V_{SW}^* are model solar wind velocities derived from the P_{SW} values predicted by bow shock models S_{BS} and H for each crossing, in conjunction with the observed electron density N_E measured by RPWS. Ion plasma moments are in preparation, so to calculate V_{SW}^* here we have assumed an electrically neutral hydrogen plasma, with N_I (ion density) = N_E. We see that most of the predicted velocities V_{SW}^*, for both models, are generally in accordance with those observed at Saturn in the past. The Pioneer 11 solar wind data considered by *Slavin et al.* [1985], for example, indicate median values for V_{SW} at Saturn of 400–500 km s^{-1}. The V_{SW}^* values predicted by both models agree to within 50 km s^{-1} for the inbound crossings. The outbound crossings, however, show a much larger discrepancy, due to the very different stand-off distances predicted by the very different shapes (eccentricities) of the bow shock models. Model H, being much more "streamlined" than S_{BS}, produces larger standoff distances, hence lower V_{SW}^* values, which are more in agreement with the inbound results. Future studies of importance should include detailed comparisons between modeled and observed solar wind speeds, using bow shock and magnetopause models and solar wind plasma data. This type of study would be valuable in assessing the timescales required for Saturn's magnetosphere to attain pressure equilibrium with the solar wind. It would also produce valuable proxy models for solar wind dynamic pressure and/or velocity.

[38] The solar wind magnetosonic Mach numbers M_S in Table 2 were calculated assuming a neutral hydrogen plasma with the CAPS measured electron temperature T_E and a characteristic ion to electron temperature ratio of T_P/T_E = 0.34, based on the large-scale empirical fit of T_E with radial distance by *Slavin and Holzer* [1981] ($T_E \propto R_{AU}^{-1/3}$), and the consistent T_P scaling laws of *Gazis and Lazarus* [1982] ($T_P \propto R_{AU}^{-0.7\pm0.2}$) and *Richardson et al.* [1995] ($T_P \propto R_{AU}^{-0.49\pm0.01}$). Relative standard deviations in solar wind temperature are typically ~40%, which translates to respective changes of ~40% and ~10% in the plasma β values and Mach numbers listed in Table 2. The formula $(V_A^2 + V_S^2)^{1/2}$ was used to calculate the magnetosonic speed, with V_A and V_S denoting Alfvén and sonic speeds respectively. These values will be revised as future ion temperature calculations become available, however they do indicate plasma flow with M_{MS} at least a factor of 2 higher than that of the terrestrial environment. The values of the plasma β parameter indicate that the bow shock of Saturn is usually in the turbulent regime (β > 1) for magnetosheath flow [*Formisano*, 1977].

4. Bow Shock Orientation

[39] In order to investigate the large-scale geometry and orientation of Saturn's bow shock, as implied by the Cassini observations, we have made use of coplanarity analysis, which by now has become a standard technique for extracting such information from single spacecraft data. The coplanarity theorem states that, for stationary, 1-D shocks, the upstream (solar wind) and downstream (magnetosheath) magnetic fields are coplanar with the local normal to the bow shock surface. In reality, planetary bow shocks do not satisfy these criteria. However, coplanarity normals provide a good first order estimate of planetary shock orientation, provided that the departure of the real bow shocks from stationarity and 1-D geometry is in some sense "small".

[40] If we consider the geometrical aspect, we note that the radius of curvature for Saturn's bow shock (in fact, for all hyperboloid shock surfaces) is $\geq L$, the size parameter, or semi-latus rectum, of the bow shock introduced in section 3. This is approximately the distance between the planet and points lying on the intersection of the dawn-dusk terminator and bow shock surface (the equality is exact if the focus of the surface is coincident with the planet center). The
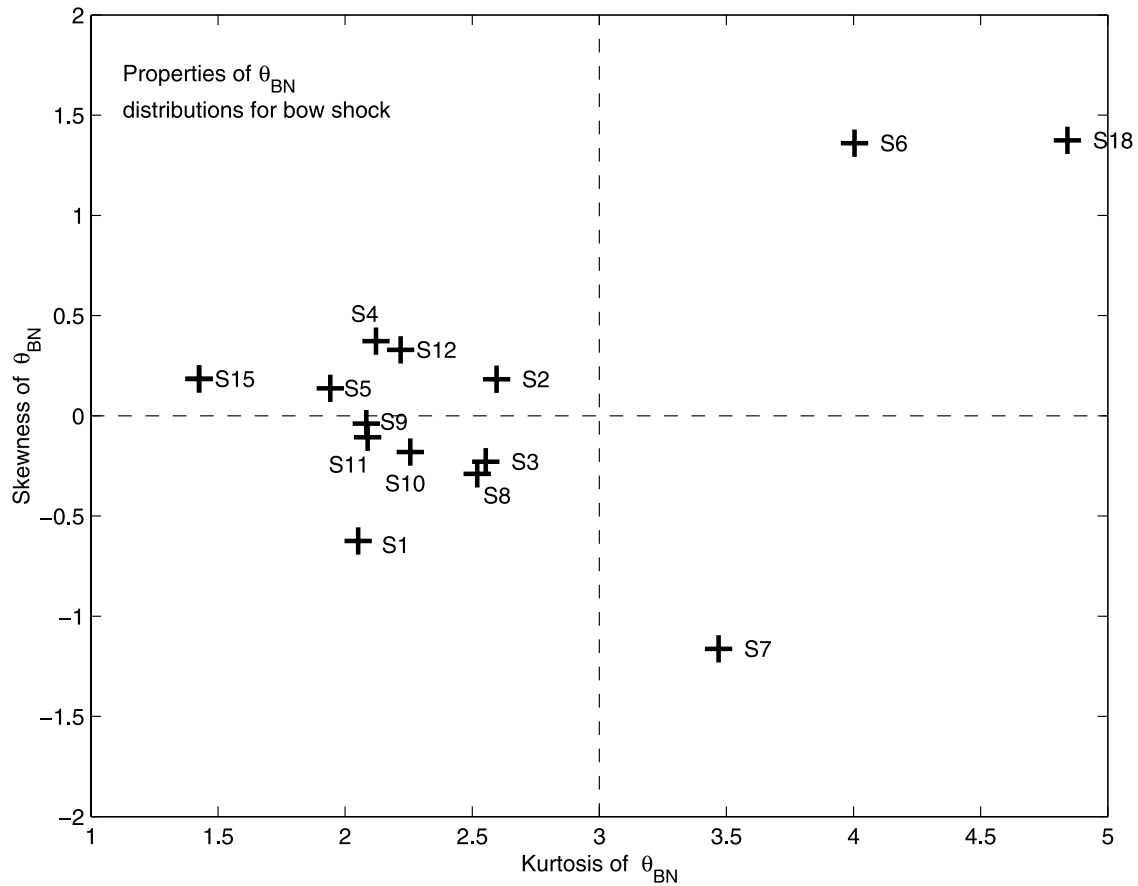
Figure 6. Statistical parameters for the distributions of shock angle θ_{BN} associated with coplanarity analysis of bow shock crossings. Skewness of each distribution is plotted versus kurtosis, with each data point labeled with the identifier of the corresponding bow shock crossing. Dotted lines indicate the parameters associated with a normal distribution (zero skewness, kurtosis equal to 3).

standoff distances in Table 1 have associated values of L between ∼35 and ∼75 R_S, and these are 2 orders of magnitude larger than the mean radii of curvature ($R_I <$ ∼20,000 km) associated with the drifting and gyrating solar wind protons upstream of Saturn's bow shock (estimated in section 5). We thus expect Saturn's shock surface to behave as a locally planar (1-D) discontinuity with respect to the spacecraft data sets used for our coplanarity analysis, which were sampled over length scales less than R_I.

[41] A quantitative measure of the deviation of the observed shock from stationarity is not as straightforward. For our coplanarity calculations, we followed the "subinterval method" described by *Gonzalez-Esparza and Balogh* [2001]. Following this technique, we selected few-minute intervals of data on the upstream (solar wind) and downstream (magnetosheath) sides of a bow shock crossing. Care was taken to avoid the overshoot region and to choose regions showing the smallest amplitude oscillations, while remaining within ∼7 min of the bow shock crossings themselves. The data intervals we used were typically ∼5 min in duration, and were extracted from magnetic time-averaged profiles with 1-s resolution, from the fluxgate magnetometer (FGM). For days 189 through 194, FGM data were not available owing to the science telemetry outage; for these days we used 4-s resolution data from the engineering telemetry stream for the VHM instrument.

[42] Following the prescribed method, we then subdivided our upstream and downstream intervals into typically eight subintervals of equal length. This gave eight estimates each for the upstream (solar wind) and downstream (magnetosheath) field components, denoted, respectively, by $\mathbf{B_U}$ and $\mathbf{B_D}$ (each estimate of field is an average taken over one subinterval). The coplanarity normal to the shock surface was derived from the usual formula,

$$\mathbf{n_{CP}} = (\mathbf{B_D} - \mathbf{B_U}) \times (\mathbf{B_D} \times \mathbf{B_U})/|(\mathbf{B_D} - \mathbf{B_U}) \times (\mathbf{B_D} \times \mathbf{B_U})|. \quad (1)$$

[43] Since we made eight estimates each (typically) for the quantities $\mathbf{B_U}$ and $\mathbf{B_D}$, we were able to compile distributions of shock angle θ_{BN} with around ∼64 elements. *Gonzalez-Esparza and Balogh* [2001] suggested that strong deviations of such distributions from a normal (Gaussian) distribution would be indicative of highly non-stationary shocks. In Figure 6, we plot the kurtosis and skewness measures associated with the coplanarity normals of the 14 suitable bow shock crossings considered in the current study. Values for these statistical parameters are, respectively, a measure of the fraction of the distribution found in the "tails" (beyond a few standard deviations from the mean) and the degree of asymmetry of the distribution about the mean value. We see that most of the crossings are more "sharply
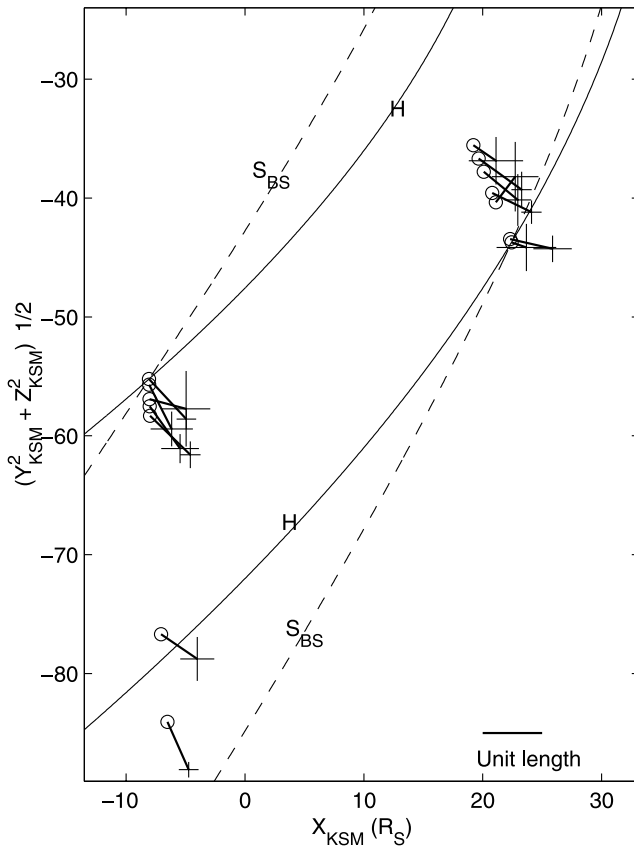
Figure 7. Projections of the coplanarity normals in the KSM cylindrical coordinates. Circles indicate locations of bow shock crossings, solid lines are vector projections with unit length shown by the scale bar. Error bars for vector components correspond to 1 standard deviation. Bow shock models S_{BS} and H (see text) have been rescaled to intersect the crossings at maximum and minimum distance from Saturn.

peaked" than a normal distribution, with kurtosis lower than 3. These are likely to be approximately stationary (insofar as they are associated with well-defined normals). The obvious exceptions, which also show the strongest deviations from symmetry about the mean (largest skewness), are crossings S6, S7 and S18. Of all the crossings on the inbound leg, S7 showed the largest downstream oscillations in field strength and direction. Between S17p and S18, CAPS observed two brief (<10 min) excursions into the magnetosheath. These observational features could be due to rapidly moving or strongly accelerating shock surfaces for which θ_{BN} effectively changed on timescales comparable to, or smaller than, the duration of the data sets considered in our coplanarity analyses.

[44] The projection of the coplanarity normals in the KSM cylindrical coordinates (described in section 3), derived for each bow shock crossing analyzed, are plotted in Figure 7. The mean normals on the earlier part of the outbound pass appear to make angles with the surface of model H that are closer to 90° than those for model S_{BS}. The angle θ_{CPM} between the coplanarity and model S_{BS} normals are shown in Figure 8, plotted against the corresponding

shock angle θ_{BN}. Most of the crossings correspond to a quasi-perpendicular shock surface ($\theta_{BN} > 45°$). S6 and S18 appear as quasi-parallel crossings, and they also showed the strongest deviations from normal θ_{BN} distributions (Figure 6). However, it is important to note that the coplanarity analysis breaks down for this type of geometry, mainly owing to the growing uncertainty in the cross product $\mathbf{B_U} \times \mathbf{B_D}$ in equation (1), which decreases toward zero for parallel shocks where $\theta_{BN} = 0$ and $\mathbf{B_U}$ and $\mathbf{B_D}$ become parallel. A similar comment applies for fully perpendicular shocks. S1, S3 and S7 coplanarity normals show the largest deviations from the model. When the standard deviations shown in Figure 8 are taken into account, the corresponding angles θ_{CPM} for model H are not significantly different from those for model S_{BS}.

[45] Figure 9 shows the ratio of downstream to upstream field strength B_D/B_U, and the shock deflection angle α (the angle between the $\mathbf{B_D}$ and $\mathbf{B_U}$ vectors). For stationary shocks in pressure equilibrium with the solar wind, these parameters are an indication of the magnetic field "jump" required to decelerate the solar wind plasma as it moves across the shock boundary into the magnetosheath. The largest errors for B_D/B_U and α are those for crossings S6 and S7, while S18 also is significantly different from the bulk of the measurements in this parameter space. This is not surprising, since these are the crossings most likely to be associated with non-stationary conditions. The rest of the crossings have field ratios between ~2 and ~5 (the maximum theoretical value from 1-D shock physics is 4), and deflection angles in the range ~10°–40°. The smallest deflection angles are indicated by crossings S8, S9, S10 – those observed on the early part of the SOI outbound pass. These small values for α (~10°) occur just before the transition SW/MS2 (Table 1), suggestive of a compressed magnetosphere. It is possible that the small deflections are due to less impeded plasma flow about a smaller magnetospheric obstacle, but this must be regarded as speculation in the absence of coincident plasma measurements.

5. Velocity and Small-Scale Structure of the Bow Shock

[46] One of the most desirable observations to be made of planetary bow shocks is the velocity of the moving shock surface itself. Not only can such measurements provide insight into the nature of the time-dependent flow of solar wind plasma around the magnetosphere, they can also be used to transform time-dependent magnetic profiles into spatial profiles. These transformed data can then give measurements of the length scales associated with the various physical features of the shock itself, such as the foot and ramp regions. Velocities of the Earth's bow shock surface have been measured using multispacecraft data. For example, *Maksimovic et al.* [2003] obtained values of the order 10–100 km s^{-1} from considering the times at which the different spacecraft in the Cluster formation crossed the same local portion of the Earth's bow shock. *Newbury and Russell* [1996] obtained speeds up to ~30 km s^{-1} for the Earth's bow shock motion via a similar analysis of data from the ISEE-1 and -2 UCLA magnetometers.

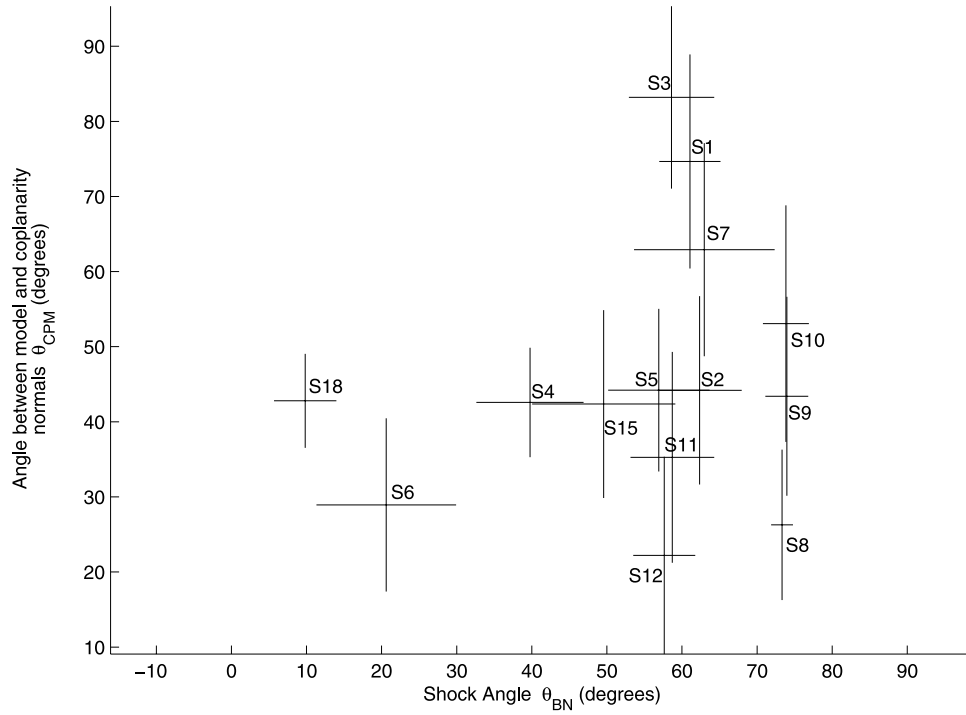[47] Cassini of course is a single spacecraft and so a different approach must be used in order to map the time

Figure 8. Angle θ_{CPM} between the computed normal vector to model S_{BS} and the coplanarity normal, plotted versus the shock normal angle from coplanarity analysis. The shock crossings corresponding to each data point are indicated by the labels. Error bars correspond to one standard deviation.
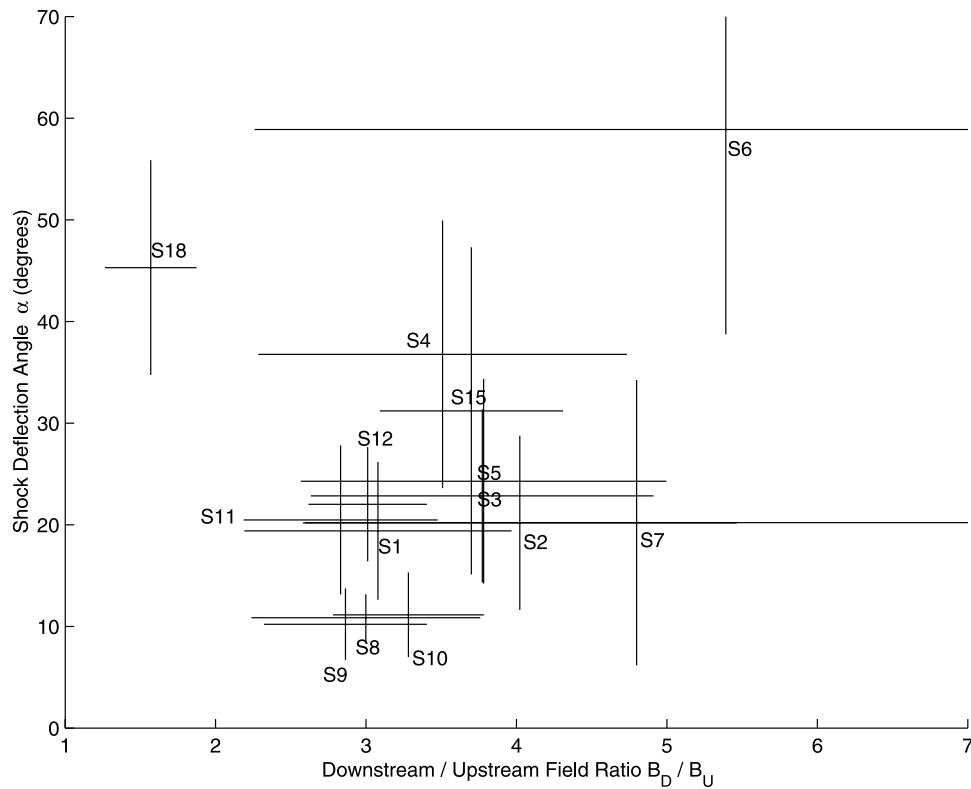

Figure 9. Shock deflection angle α (see text) versus ratio of downstream to upstream magnetic field for the labeled shock crossings. Error bars indicate 1 standard deviation.

series of magnetic field measurements into spatial profiles. The method we have used herein is to assume a theoretical length scale for the shock foot region of Saturn, and then "work backward" in order to derive: (1) the required shock speed V_{SH} and (2) the length scale for the ramp region of the observed shock crossings.

[48] The calculations of *Gosling and Thomsen* [1985] resulted in the following expression for the perpendicular distance from an oblique (1-D) shock at which an incident ion "turns around" after having been specularly reflected from the shock ramp.

$$d = (V_U/\Omega_U)\left[\psi\left(2\,\cos^2\theta - 1\right) + 2\,\sin^2\theta\sin\psi\right]$$
$$\cos\psi = (1 - 2\,\cos^2\theta)/(2\,\sin^2\theta) \tag{2}$$

where V_U is the incident velocity component of the ion perpendicular to (and in the rest frame of) the local shock surface, Ω_U is the upstream (solar wind) ion (angular) gyrofrequency, and θ is equal to θ_{BN}, the shock angle between the solar wind magnetic field and the shock normal. Equation (2) has been widely used for determining shock velocity from single spacecraft measurements. It can only be evaluated for shocks having $\theta_{BN} > 30°$. For smaller θ_{BN}, there is no real solution for $\cos\psi$ and the ions do not turn around, but escape upstream. Changing θ_{BN} from 30° to 90° (fully perpendicular shock) decreases the angular factor multiplying the ion convective gyroradius (V_U/Ω_U) from ~1.57 to ~0.68. In this context, it is important to realize that more sophisticated models and numerical simulations of the ion reflection process at the bow shock have revealed that it is more complex than originally suggested by the specular reflection model, with the detailed behavior of shock foot thickness (equivalent to the turnaround distance d) depending on additional factors, such as the properties of the particle distribution and multiple reflections [e.g., *Gedalin*, 1996; *Wilkinson*, 1991; *Wilkinson and Schwartz*, 1990]. For our estimates herein of the order of magnitude of the shock foot thickness (length scale), we have used equation (2); this degree of approximation is reasonable according to the observations of *Newbury and Russell* [1996].

[49] Our sample of bow shock observations are mostly quasi-perpendicular with a well-defined shock foot signature (we return to this point later). However, we must treat our calculations of the shock foot durations in time as first-order estimates. This is partly because of the high plasma β parameter implied by the CAPS observations (Table 2), which imply a high-velocity dispersion for the solar wind ions (ion thermal velocity up to ~20% of our assumed value of 400 km s^{-1} for the total solar wind speed V_{SW}). The turnaround distance d occupies a corresponding range of values.

[50] The other sources of uncertainty are related to the observational determination of the shock foot's upstream edge. Because d is measured perpendicular to the shock surface, its extraction from magnetic data relies on accurate shock normals, and on a reliable signature of the commencement of the shock foot region. We aim to use forthcoming ion plasma data in future studies to refine the latter requirement, in particular.

[51] For the present estimates, we located the shock foot boundary in time by starting at the upstream solar wind intervals, used for calculating mean solar wind field $\mathbf{B_U}$ used in our coplanarity calculations. We then considered points increasingly closer to the bow shock crossing until the field magnitude exceeded $B_U + 4\sigma_B$, i.e., 4 standard deviations above the initial mean solar wind field. This criterion was chosen to help ensure the identification of a time t_f where the magnetic field had begun to significantly increase, compared to the nominal upstream field strength B_U. Unusually disturbed solar wind data made this type of shock foot identification impossible, and were not used. The time t_{rs} of the upstream boundary of the shock ramp was then determined, by means of fitting a linear function to the ramp itself and setting t_{rs} equal to the time at which this function became equal to the upstream field strength B_U. The time duration for the shock foot, as observed by the spacecraft, was then set to $\Delta t = |t_f - t_{rs}|$. The shock foot's thickness d is related to its observed duration by

$$d = |\mathbf{v_{SC}} \cdot \mathbf{n} - V_{SH}|\Delta t \quad , \tag{3}$$

where $\mathbf{v_{SC}}$ is the spacecraft velocity measured in the KSM system where Saturn is at rest. In this system, the shock velocity component V_{SH} along the direction of the shock normal $\mathbf{n}$ was calculated by substituting the theoretical expression for d from equation (2). The model normals from the bow shock model S_{BS} (section 4) were used, however the order of magnitude of the results was insensitive to the choice of model or coplanarity normals.

[52] Figures 10 and 11 show the magnetic profiles for the first six bow shock crossings observed by Cassini at Saturn, as both time series and as spatial profiles. The spatial scales are in units of the upstream ion inertial length. This length and the ion convective gyroradius (in the shock rest frame) were computed using the RPWS plasma moments in Table 2, along with the MAG values of mean upstream magnetic field B_U used for the coplanarity analysis (section 4). The values for both parameters are listed in Table 3.

[53] The magnetic profiles generally show high levels of turbulence in the downstream region, often giving the appearance of "multiple" crossing structures. This is most likely a result of the relatively high plasma β observed in the solar wind, linked with turbulence downstream. The ion inertial length emerges as the scale length for the shock ramp region. The width from the ramp's upstream edge to the overshoot is ~1 to ~3 ion inertial lengths. To consider the ramp alone, we estimated its downstream edge as the time point where the ramp linear fit equaled the mean downstream field B_D used in the coplanarity normal calculations, and representative of the magnetosheath beyond the overshoot structure. The ramp thickness was then obtained by using equation (3), substituting the ramp duration for Δt. The results for the inbound crossings (for which ion inertial lengths could be computed) are shown in Table 3. The ramp widths are of the order between a tenth and one ion inertial length. Considering the location of the shock foot edge is a first-order estimate using magnetic field data alone, and that we have had to assume a value for the solar wind speed, these results are in good agreement with the observations of *Newbury and Russell* [1996] that the ion inertial length upstream of the Earth's bow shock is the length scale for its
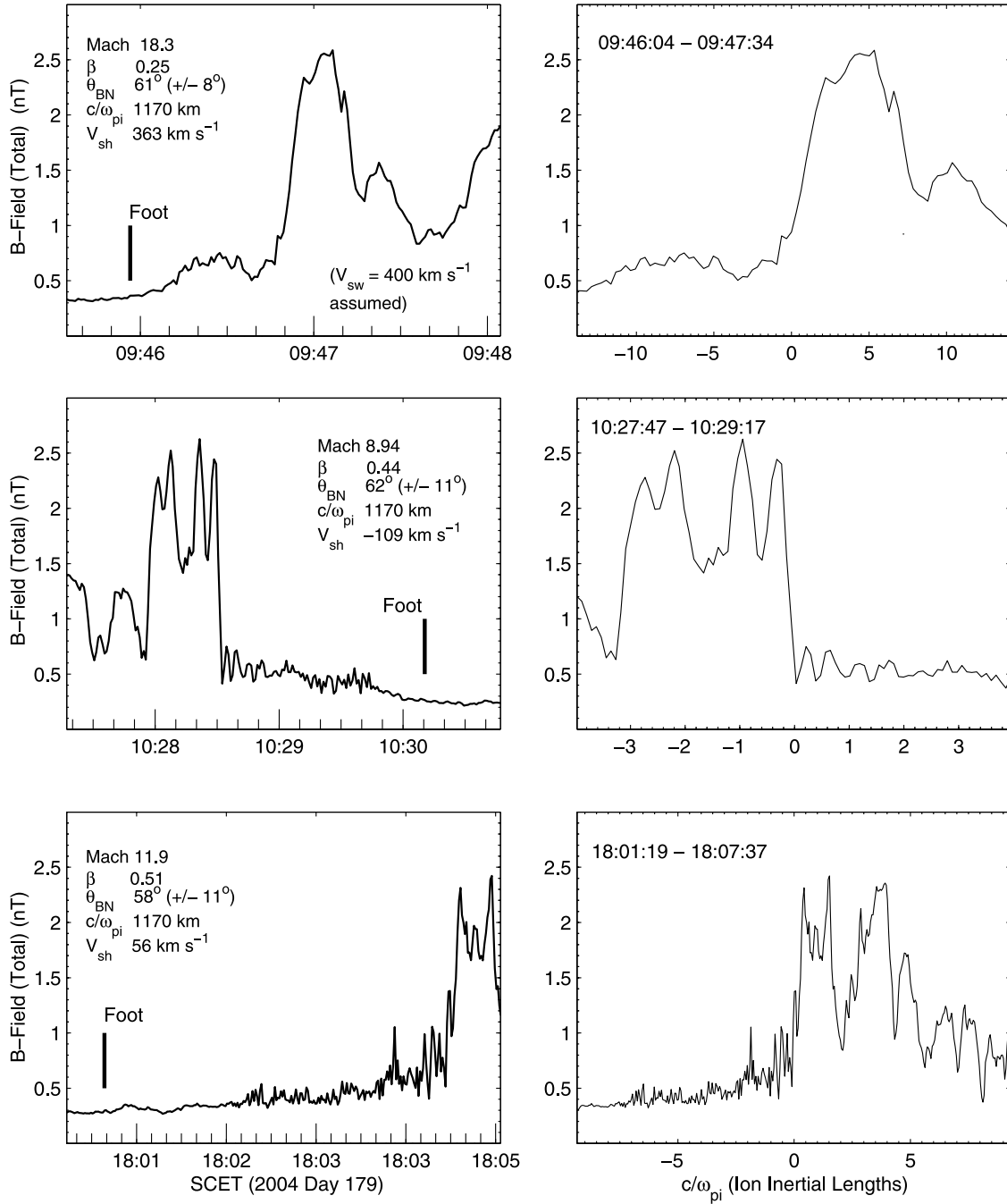
Figure 10. (left) Magnetic profiles for Cassini bow shocks (top) S1, (middle) S2, and (bottom) S3 as a function of time. (right) Magnification of the crossings, plotted as field strength versus position perpendicular to the shock surface, in units of ion inertial length. Upstream plasma parameters and estimated shock foot edges are shown. Effective Mach number in the shock rest frame is indicated (see text).

ramp region. This supports the picture of ion kinetics determining the magnetic profiles of Saturn's bow shock, and playing a role in its energy dissipation.

[54] We now consider the shock speeds derived from the analyzed crossings listed in Table 3. They are of the order $10-100$ km s^{-1} It is worth noting that the coplanarity analysis for S6 predicted $\theta_{BN} \sim 20°$ which corresponds to an "infinitely large" shock foot, according to the angular factor appearing in equation (2) above. We have therefore

used a value of $\theta_{BN} \sim 40°$ for calculation of V_{SH} for S6, which is the largest angle consistent with its coplanarity analysis.

[55] For purposes of further analyzing shock dynamics, we have calculated the "effective" Mach numbers M_{MS}^* for the inbound shock crossings (for which plasma moments were available). These are the Mach numbers based on the flow of the solar wind perpendicular to the shock surface in the frame of reference where the shock is at rest. In other
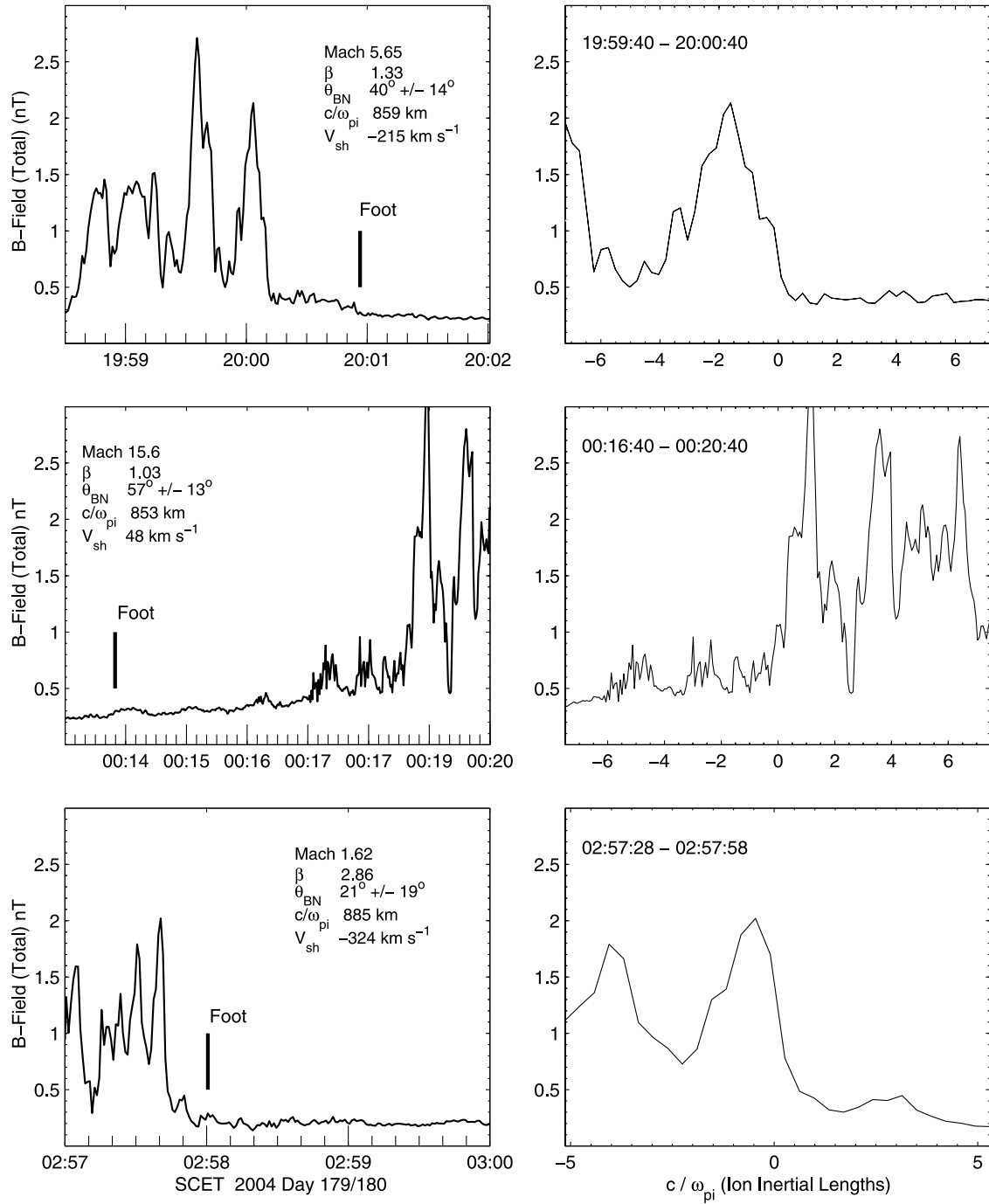
Figure 11. (left) Magnetic profiles for Cassini bow shocks (top) S4, (middle) S5, and (bottom) S6 as a function of time. (right) Magnification of the crossings, plotted as field strength versus position perpendicular to the shock surface, in units of ion inertial length. Upstream plasma parameters and estimated shock foot edges are shown. Effective Mach number in the shock rest frame is indicated (see text).

words, the frame where the component of the solar wind flow perpendicular to the shock surface is $V_{SW} \cos\gamma + V_{SH}$. We assumed $V_{SW} = -400$ km s^{-1} (using the sign convention in Table 3) as for our other analyses and obtained the angle γ between the shock normal and the solar wind direction by using the geometry of shock surface model S$_{BS}$ by *Slavin et al.* [1985], introduced in section 3. The results are shown in Figure 12, where the values M$^*_{MS}$ are plotted against the

relative overshoot amplitude of each crossing. The latter was defined as $(B_M - B_D)/B_D$, where B_D is the representative value of the downstream (magnetosheath) field used in the coplanarity analysis (section 4) and B_M is the peak value of the field strength in the overshoot region. The plot also shows B_M versus effective Mach number.

[56] The necessarily small sample size of shock crossings used for the graph, and the lack of definitive solar wind

Table 3. Ion Inertial Lengths and Ion Convective Gyroradii Upstream of Bow Shock Crossings Listed, Computed From CAPS ELS Solar Wind Plasma Moments[a]

Label and UTC of Crossing (Upstream Ramp Edge)	Ion Inertial Length, km	Ion Convective Gyroradius, km	V_{SH} (With V_{SW} = 400 km s^{-1})	Shock Ramp Width (Ion Inertial Lengths)
S1 2004D179T09:46:49	1170	24111	363	1.11
S2 2004D179T10:28:32	1170	12478	−109	0.13
S3 2004D179T18:04:28	1170	17041	56	0.29
S4 2004D179T20:00:10	859	7202	−215	0.72
S5 2004D180T00:18:40	853	18521	48	0.38
S6 2004D180T02:57:42	885	2691	−324	0.39
S7 2004D180T05:37:50	814	25392	103	2.74
S8 2004D189T14:05:45	...	6370	−31	...
S9 2004D189T16:15:11	...	9211	176	...
S10 2004D189T21:46:49	...	4767	−66	...
S11 2004D190T00:30:55	...	5745	18	...
S12 2004D190T04:13:27	...	4515	−32	...
S15 2004D194T05:11:36	...	15033	−69	...

[a]CAPS ELS solar wind plasma moments are from Table 2. Shock velocity (km s^{-1}) at each crossing (positive outward from Saturn) and shock ramp width in units of ion inertial length are also shown.

velocity observations, do not allow us to comment with any confidence on the existence of any correlation between overshoot size and effective Mach number. *Russell et al.* [1982] established that the overshoot size in supercritical quasi-perpendicular bow shocks was positively correlated with Mach number and plasma beta. This study used an extensive magnetic and plasma data set for the Earth, Jupiter and Saturn. A similar study or confirmation of this result using Cassini data would be desirable as more extensive and definitive data sets are calibrated and become available. We note the marginally supermagnetosonic Mach number M^*_{MS} for the shock crossing S6 in Figure 12, which is consistent with the fact that it has the weakest overshoot of the observed crossings.

[57] We can also note that all of the crossings from S3 through to S14 occur in natural "pairs" where the first crossing in each pair (solar wind to magnetosheath) corresponds to a high effective Mach number (outward moving shock) and a relatively large overshoot, while the second crossing occurs when the shock is moving inward, and so the Mach number and overshoot amplitude are reduced. The larger overshoots correspond to a shock which dissipates the higher kinetic energy carried by solar wind plasma which moves at higher speed in the rest frame of the shock.

[58] The described assumptions we have adopted for our analysis do not allow us to treat the derived shock velocities and dependent parameters as anything more than order of magnitude estimates. To this level of approximation, the shock velocities for Saturn are at least of the same order as those derived for the Earth's shock by, for example, *Maksimovic et al.* [2003] and *Newbury and Russell* [1996]. The relative responses of the Earth's and Saturn's magnetospheres to variation in solar wind pressure mainly depend on planetary magnetic field strength and geometry, and magnetospheric plasma content. The relative timescales required to achieve dynamic equilibrium between the magnetosphere/magnetosheath and the solar wind also may play a role. Future correlative studies of magnetic and plasma data should help to provide a more accurate comparison between the shock dynamics of the two planets.

[59] An important feature of Table 3 is the fact that positive (outward from Saturn) velocities of the shock are associated with shock transitions progressing in time from the solar wind to the magnetosheath, while motions of the bow shock toward Saturn (negative V_{SH}) occur at the positions where the spacecraft exits from the magnetosheath and enters the solar wind. The nature of the shock encounters is thus dominated by the motions of the bow shock itself. The velocity of the space craft is not important in this context at these distances from Saturn, since it is ∼5 km s^{-1}, generally small compared to the V_{SH} values calculated. It follows that on the timescale of the intervals between the bow shock crossings, the shock velocities are suggestive of motion with an oscillatory character, with a period of about 6 hours.

6. Summary and Conclusions

[60] We have considered observations of Saturn's bow shock (and magnetopause) boundary by the Cassini spacecraft, with the aim of a description of the large- and small-scale structure of the bow shock and magnetopause, as well as an order-of-magnitude estimate of the velocity of the shock surface itself. These physical properties are essential for studies of magnetospheric dynamics and the magnetosphere−solar wind interaction.

[61] By using geometrical models for the bow shock and magnetopause, on the basis of both empirical and theoretical techniques (section 3), we found that the location and distribution of the bow shock crossings was indicative of at least one magnetospheric compression event which occurred during Cassini's traversal of the magnetosphere. This is in agreement with the conclusions of *Dougherty et al.* [2005] (from a general comparison with previous flybys) and *Jackman et al.* 2005] (from a study of the behavior of the IMF at times encompassing the SOI interval). Specifically, our modeling shows evidence for an increase in solar wind dynamic pressure for this compression event by at least a factor of ∼2−5. This was followed on the outbound pass by an expansion of the system, back toward a configuration close to that originally detected on the inbound leg. The standoff distance of the bow shock changed signifi-
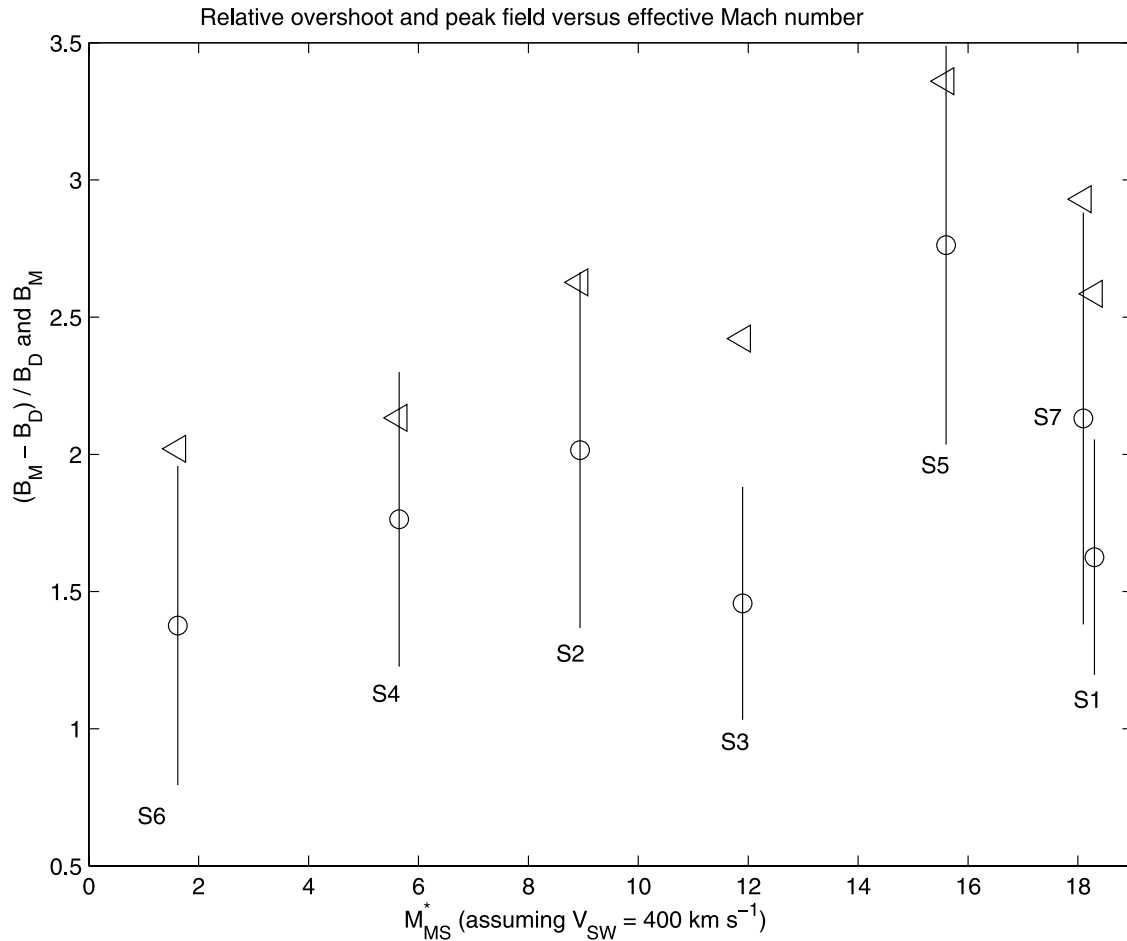
Figure 12. Relative overshoot (circles) in magnetic field strength and maximum field (triangles) in nano-Tesla at overshoot region, versus effective Mach number, for the inbound shock crossings. Vertical bars indicate uncertainty in relative overshoot, based on the variance of the downstream field.

cantly during this time, by $\sim$10 R_S, comparable to the standoff distance itself (20–35 R_S).

[62] We then performed a coplanarity analysis of the shock crossings, mainly to determine the shock angle θ_{BN} between the solar wind field and the shock normal. Most of the crossings observed (12 out of 14) were quasi-perpendicular ($\theta_{BN} > 45°$) and, of these, three showed θ_{BN} distributions markedly different from the normal statistical type, probably a signature of a nonstationary shock [*Gonzalez-Esparza and Balogh*, 2001]. The angle θ_{CPM} between the coplanarity normals and the shock model normals used in this study was consistent with a value <40° for 11 of the 14 cases. In light of the inherent limitations of coplanarity analysis, these results support the shock models used as a reasonable representation of the global geometry of the Saturn bow shock, although future analyses of this nature with more Cassini orbits is required in order to constrain models further. The crossings which had $\theta_{CPM} > 40°$ included one of the probable nonstationary cases. The spread in θ_{CPM} was greatest for crossings with $\theta_{BN} \sim 60°$.

[63] Finally, we examined the small-scale structure and velocity of the bow shock at Saturn as revealed by the magnetic profiles and available electron plasma data. We assumed a bow shock geometry consistent with the model S_{BS} [*Slavin et al.*, 1985, section 4] and a total solar wind

speed of 400 km s^{-1}. We then used the theoretical value of the shock foot thickness by *Gosling and Thomsen* [1985] and the observed duration in time of the magnetic foot region to derive a shock velocity at 13 bow shock crossings. This also allowed us to estimate the length scale of the shock ramp region, which plays a central role in the ion refection processes that generates the shock foot (see, e.g., the review by *Gedalin* [1997]).

[64] The shock velocities obtained were of the same order of magnitude as those observed at the Earth using multispace-craft data [e.g., *Newbury and Russell*, 1996; *Maksimovic et al.*, 2003]. Future magnetic/plasma correlative studies are essential for obtaining more results of this nature. The length scale for Saturn's shock ramp was of the order 0.1–1 ion inertial lengths. The equivalent parameter at the Earth sets the scale for the Earth's shock ramp. This result indicates that Saturn's quasi-perpendicular bow shock is the site of energy dissipation processes largely controlled by ion kinetics, as for the case of the Earth. This is despite the fact that Saturn's bow shock has much higher upstream Mach numbers ($\sim$10–15, section 5) and upstream plasma β (< $\sim$4, section 5), the latter placing it in the nonlaminar flow regime.

[65] The results of this study compare quite well, in general, with those of *Smith et al.* [1980b] who analyzed

Pioneer magnetospheric observations of Saturn. In both cases, the bow shock was observed to be typically quasi-perpendicular. The shock speeds are comparable, of the order $10-100$ km s^{-1}, although different methods of determination were used. The shock thickness for both studies are comparable; the Pioneer analysis derived a thickness of a few ion inertial lengths, somewhat larger than Cassini.

References

Burgess, D. (1995), Collisionless shocks, in *Introduction to Space Physics*, edited by M. G. Kivelson and C. T. Russell, pp. 129–163, Cambridge Univ. Press, New York.

Connerney, J. E. P., M. H. Acuna, and N. F. Ness (1983), The Z3 zonal harmonic model of Saturn's magnetic field: Analysis and implications, *J. Geophys. Res.*, *88*, 8771.

Dougherty, M. K., et al. (2004), The Cassini Magnetic Field Investigation, *Space Sci. Rev.*, *114*, 331.

Dougherty, M. K., et al. (2005), Cassini magnetometer observations during Saturn orbit insertion, *Science*, *307*, 1266.

Farris, M. H., C. T. Russell, M. F. Thomsen, and J. T. Gosling (1992), ISEE-1 and -2 observations of the high beta shock, *J. Geophys. Res.*, *97*, 19,121.

Formisano, V. (1977), The physics of the Earth's collisionless shock wave, *J. Phys.*, *38*, suppl. 12, C6–65.

Gazis, P. R., and A. J. Lazarus (1982), Voyager observations of solar wind proton temperature: 1-10 AU, *Geophys. Res. Lett.*, *9*, 431.

Gedalin, M. (1996), Ion reflection at the shock front revisited, *J. Geophys. Res.*, *101*, 4871.

Gedalin, M. (1997), Ion dynamics and distribution at the quasi-perpendicular collisionless shock front, *Surv. Geophys.*, *18*, 541.

Gonzalez-Esparza, J. A., and A. Balogh (2001), The θ_{BN} problem: Determination of the shock local magnetic parameters from in-situ IMF data, *Geofis. Int.*, *40*, 53.

Gosling, J. T., and M. F. Thomsen (1985), Specularly reflected ions, shock foot thicknesses, and shock velocity determinations in space, *J. Geophys. Res.*, *90*, 9893.

Gurnett, D. A., et al. (2004), The Cassini radio and plasma wave investigation, *Space Sci. Rev.*, *114*, 395.

Hendricks, S., F. M. Neubauer, M. K. Dougherty, N. Achilleos, and C. T. Russell (2005), Variability in Saturn's bow shock and magnetopause from Pioneer and Voyager: Probabilistic predictions and initial observations by Cassini, *Geophys. Res. Lett.*, *32*, L20S08, doi:10.1029/2005GL022569.

Jackman, C. M., N. Achilleos, E. J. Bunce, S. W. H. Cowley, and S. E. Milan (2005), Structure of the IMF during first Cassini fly-through of Saturn's magnetosphere, *Adv. Space Res.*, *20*, 2120.

Joy, S. P., M. G. Kivelson, R. J. Walker, K. K. Khurana, C. T. Russell, and T. Ogino (2002), Probabilistic models of the Jovian magnetopause and bow shock locations, *J. Geophys. Res.*, *107*(A10), 1309, doi:10.1029/ 2001JA009146.

Kennel, C. F., J. P. Edmiston, and T. Hada (1985), A quarter century of collisionless shock research, in *Collisionless Shocks in the Heliosphere:*

A Tutorial Review, *Geophys. Monogr. Ser.*, vol. 34, edited by R. G. Stone and B. T. Tsurutani, p.1–36, AGU, Washington, D. C.

Lepping, R. P., L. F. Burlaga, and F. W. Klein (1981), Surface waves on Saturn's magnetopause, *Nature*, *292*, 750.

Maksimovic, M., S. D. Bale, T. S. Horbury, and M. André (2003), Bow shock motions observed with Cluster, *Geophys. Res. Lett.*, *30*(7), 1393, doi:10.1029/2002GL016761.

Maurice, S., I. M. Engle, M. Blanc, and M. Skubis (1996), Geometry of Saturn's magnetopause model, *J. Geophys. Res.*, *101*, 27,053.

Newbury, J. A., and C. T. Russell (1996), Observations of a very thin collisionless shock, *Geophys. Res. Lett.*, *23*, 781.

Petrinec, S., and C. T. Russell (1997), Hydrodynamic and MHD equations across the bow shock and along the surfaces of planetary obstacles, *Space Sci. Rev.*, *79*, 757.

Richardson, J. D., K. I. Paularena, A. J. Lazarus, and J. W. Belcher (1995), Radial evolution of the solar wind from IMP 8 to Voyager 2, *Geophys. Res. Lett.*, *22*, 325.

Russell, C. T., and E. W. Greenstadt (1979), Initial ISEE magnetometer results: Shock observations, *Space Sci. Rev.*, *23*, 3.

Russell, C. T., M. M. Hoppe, and W. A. Livesey (1982), Overshoots in planetary bow shocks, *Nature*, *296*, 45.

Savoini, P., and B. Lembege (1994), Electron dynamics in two- and one-dimensional oblique supercritical collisionless magnetosonic shocks, *J. Geophys. Res.*, *99*, 6609.

Scudder, J. D., A. Mangeney, C. Lacombe, C. C. Harvey, T. L. Aggson, R. R. Anderson, J. T. Gosling, G. Paschmann, and C. T. Russell (1986), The resolved layer of a collisionless, high β, supercritical quasi-perpendicular shock wave: 1. Rankine-Hugoniot geometry, currents, and stationarity, *J. Geophys. Res.*, *91*, 11,019.

Slavin, J. A., and R. E. Holzer (1981), Solar wind flow about the terrestrial planets: 1. Modeling bow shock position and shape, *J. Geophys. Res.*, *86*, 11,401.

Slavin, J. A., E. J. Smith, J. R. Spreiter, and S. S. Stahara (1985), Solar wind flow about the outer planets: Gas dynamic modeling of Jupiter and Saturn bow shocks, *J. Geophys. Res.*, *90*, 6275.

Smith, E. J., L. Davis Jr, D. E. Jones, P. J. Coleman Jr, D. S. Colburn, P. Dyal, and C. P. Sonett (1980a), Saturn's magnetosphere and its interaction with the solar wind, *J. Geophys. Res.*, *85*, 5655.

Smith, E. J., L. Davis Jr, D. E. Jones, P. J. Coleman Jr, D. S. Colburn, P. Dyal, and C. P. Sonett (1980b), Saturn's magnetic field and magnetosphere, *Science*, *207*, 407.

Walker, R. J., and C. T. Russell (1995), Solar-wind interactions with magnetized planets, in *Introduction to Space Physics*, edited by M. G. Kivelson and C. T. Russell, pp. 164–181, Cambridge Univ. Press, New York.

Wilkinson, W. P. (1991), Ion kinetic processes and thermalization at quasi-perpendicular low-Mach number shocks, *J. Geophys. Res.*, *96*, 17,675.

Wilkinson, W. P., and S. J. Schwartz (1990), Parametric dependence of the density of specularly reflected ions at quasiperpendicular collisionless shocks, *Planet. Space Sci.*, *38*, 419.

Young, D. T., et al. (2004), Cassini plasma spectrometer investigation, *Space Sci. Rev.*, *114*, 1.

————————————

N. Achilleos, C. S. Arridge, C. Bertucci, and M. K. Dougherty, Blackett Laboratory, Imperial College London, SW7 2AZ, U. K. (n.achilleos@ imperial.ac.uk)

M. E. Burton, E. J. Smith, and B. T. Tsurutani, Jet Propulsion Laboratory, California Institute of Technology, Pasadena, CA 91109, USA.

S. Hendricks, Institute of Geophysics and Meteorology, University of Cologne, Cologne D-50923, Germany.

G. B. Hospodarsky, Department of Physics and Astronomy, University of Iowa, Iowa City, IA 52242, USA.

C. T. Russell, UCLA Institute of Geophysics and Planetary Physics, Los Angeles, CA 90024, USA.

A. M. Rymer, Mullard Space Science Laboratory, University College London, WC1E 6BT, U. K.